Experimental Characterization and Modeling Stiffness of Polymer/Clay Nanocomposites within a Hierarchical Multiscale Framework

A. Mesbah,[1,2] F. Zaïri,[1] S. Boutaleb,[1,2] J. M. Gloaguen,[3] M. Naït-Abdelaziz,[1] S. Xie,[3] T. Boukharouba,[2] J. M. Lefebvre[3]

[1]*Laboratoire de Mécanique de Lille (UMR CNRS 8107), USTL, Polytech'Lille, Avenue P. Langevin, Villeneuve d'Ascq Cedex 59655, France*
[2]*Laboratoire de Mécanique Avancée, USTHB, BP32 El-Alia Bab-Ezzouar, Alger 16111, Algeria*
[3]*Laboratoire de Structure et Propriétés de l'Etat Solide (UMR CNRS 8008), USTL, Bât. C6, Villeneuve d'Ascq Cedex 59655, France*

Received 15 August 2008; accepted 5 April 2009
DOI 10.1002/app.30547
Published online 7 August 2009 in Wiley InterScience (www.interscience.wiley.com).

ABSTRACT: To provide a better understanding of the relationship between nanostructure and overall material stiffness in the case of polymer/clay nanocomposites, both analytical and finite element modeling were considered. A micromechanical analytical approach based on a multiscale framework is presented in which special attention is devoted to the constrained region around reinforcements. The thickness of the constrained region is seen as a characteristic length scale and the effect of particle size is explicitly introduced in the model. Moreover, the constrained region presents graded properties. The hierarchical morphology of intercalated silicate stacks is also explicitly introduced in the micromechanical model from an equivalent stiffness method in which the silicate stacks are replaced by homogeneous particles with constructed equivalent anisotropic stiffness. The orientational averaging process is used to derive the overall stiffness tensor of nanocomposite materials containing randomly oriented reinforcements. The respective influence of volume fraction, aspect ratio, size and orientation of the reinforcements, matrix properties, number of silicate layers per stack, and interlayer spacing on the overall nanocomposite stiffness is analyzed. The overall stiffness of polymer/clay nanocomposite systems is also evaluated by means of finite element simulations and the results compare favorably with model predictions. From an experimental point of view, relevant morphological and mechanical data were obtained on polyamide-6 nanocomposites prepared using a modified montmorillonite Cloisite 30B and an unmodified sodium montmorillonite Cloisite Na^+. The amount of constrained region around reinforcements was estimated using results issued from dynamic mechanical analyses and differential scanning calorimetry. Comparison to the model clearly underlines the contribution of the constrained region to the stiffness improvement. J Appl Polym Sci 114: 3274–3291, 2009

Key words: nanocomposites; nanoclay; inhomogeneous interphase; micromechanical modeling; finite element analysis

INTRODUCTION

Since the pioneering work of Usuki et al.[1] and Kojima et al.,[2] polymer/clay nanocomposites have received considerable attention in literature. It was shown that the mechanical properties of polyamide-6 were significantly improved at low weight fractions of clay. For instance, a 4.7% clay weight fraction results in an increase of both elastic modulus and strength by a factor two. The stiffening effect of nanoclay particles is generally explained in terms of high interactions with polymer matrix, perfect alignment, small aspect ratio ($\ll 1$), and small dimensions.[3–6] Clay platelets dimensions lead to both a large specific surface area and a small interparticle distance of the order of characteristic polymer length scale. Moreover, clay exhibits a high modulus compared with that of the surrounding polymer matrix. Polymer/clay nanocomposites may be described with respect to the state of clay dispersion into the matrix: (i) in its original aggregated state, in which case, we rather deal with a microcomposite; (ii) in an intercalated state, in which a layered structure consisting of several clay platelets is preserved; and (iii) in an exfoliated state where clay platelets are individually dispersed in the matrix. The optimal enhancement of mechanical properties requires a fully exfoliated state. To improve clay dispersion, various elaboration methods were attempted, including the use of surfactants and the processing conditions (melt mixing, in situ polymerization, etc.). In most cases, an ammonium-based organic surfactant

Correspondence to: F. Zaïri (fahmi.zairi@polytech-lille.fr).

is used to favor the intercalation of the polymer between clay platelets.[3–6] The major difference between nanocomposites and composites with microsized particles is the influence of the interphase. Indeed, the existence of a constrained region around the silicate at the nanometer scale because of the perturbation of the molecular structure of polymer matrix is widely mentioned in the literature.[2] This constrained region pertains to the same length scale as that of the nanoparticle and its properties are expected to be different from those of the bulk matrix. The influence of the constrained region increases with the level of clay dispersion.

Most investigations on nanocomposites have been focused on materials processing, microstructural characterization, and macroscopic property measurements.[3–6] Enhancement of physical properties (e.g., barrier resistance, thermal properties, and ablation performance) was a subject of extensive studies. Since the work of Usuki et al.[1] and Kojima et al.,[2] many experimental investigations have shown a significant increase in mechanical properties of polymer/clay nanocomposites.[3–6] As a consequence, establishing predictive tools is a fundamental task for an accurate understanding of mechanical property enhancement in this class of materials.

Recent studies have proposed micromechanical modeling to analyze elastic properties of polymer/clay nanocomposites. Kojima et al.[2] used the rule of mixtures to estimate the elastic modulus of polyamide-6/clay nanocomposites. The elastic modulus of the same system was predicted by Masenelli-Varlot et al.[7] based on Voigt approximation and Tandon-Weng[8] approach. Brune and Bicerano[9] relied on the Halpin-Tsai[10] equation to qualitatively examine the effect of incomplete exfoliation and imperfect alignment of the platelets on the stiffness of nanocomposites. The effect of incomplete exfoliation was also investigated by Luo and Daniel[11] using the Mori-Tanaka[12] model. In this approach, the hierarchical nature of intercalated silicate stacks was taken into account by considering the nanoparticle as a laminate-like structure. This methodology was also used by Sheng et al.[13] using the Mori-Tanaka model and was termed "effective clay particle concept" by the authors. The anisotropic nature of the silicate was taken into consideration by Wang and Pyrz.[14] In their analysis based on the Mori-Tanaka model, they found that the degree of anisotropy of the silicate has an insignificant effect on the overall stiffness of nanocomposites. The elastic modulus and volume fraction of the constrained region adjacent to the silicate for a polyamide-6/clay nanocomposite were estimated by Shelley et al.[15] based on the rule of mixtures. The elastic modulus of the constrained region in the same system was estimated by Ji et al.[16] using a parallel-series model. The analytical predictions of Wang and Pyrz[17] based on the Mori-Tanaka approach were found very close to the experimental data for various polymer/clay nanocomposites without taking into consideration the constrained region. The authors concluded that the constrained region is apparently not a stiffening parameter. This review is not exhaustive and many other papers used conventional micromechanical models (rule of mixtures, Halpin-Tsai and Mori-Tanaka) to predict the overall stiffness of polymer/clay nanocomposites.[18–24] The effectiveness of finite element (FE) method to evaluate nanocomposite stiffness was also recently pointed out.[13,25,26] These investigations show that these models, widely used for microcomposites, may provide satisfactory predictions of the nanocomposite stiffness. However, these studies do not consider the influence of particle size. Moreover, the inhomogeneous nature of the constrained region was not taken into account.

In the present article, polyamide-6 nanocomposites with two clay weight fractions (2 and 5%) were produced using an organoclay (Cloisite 30B) and an unmodified clay (Cloisite Na^+). Clay dispersion in nanocomposites was assessed by transmission electron microscopy. The viscoelastic (glassy to rubbery) response of neat polyamide-6 and its nanocomposites was characterized by dynamic mechanical analysis. The fraction of constrained region around reinforcements was quantified and the effect of the nature and amount of clay was studied. Tensile tests were also performed at room temperature. A micromechanical modeling is presented to predict the stiffness tensor of nanocomposite materials. To reach this goal, a multiscale approach is used in which both the morphology of intercalated silicate stacks and the existence of constrained region are taken into account. The nanocomposite is, therefore, modeled as a three-phase composite consisting of nanoparticles, interphase surrounding the nanoparticles and polymer matrix. The incorporation of an interphase to model the constrained region allows to account for an internal material length and the effect of particle size. The interphase is assumed to have nonuniform mechanical properties. The hierarchical morphology of particles is considered according to an equivalent stiffness method in which the silicate stacks are replaced by homogeneous particles with constructed equivalent anisotropic stiffness. The stiffness of an intercalated silicate stack, seen as a parallel platelet system, is calculated using laminate theory. The overall stiffness of nanocomposites containing randomly oriented reinforcing elements is obtained through the averaging process over all orientations. The respective influence of several parameters, such as volume fraction, aspect ratio, size and orientation of the reinforcements, matrix properties, number of silicate layers per stack, and interlayer

spacing, on stiffness enhancement of polymer/clay nanocomposites is investigated. Finite element analysis is also performed to evaluate the overall nanocomposite stiffness. Comparisons between the results from the micromechanical analytical model and experimental data are considered for both exfoliated and intercalated nanocomposites.

EXPERIMENTAL

Materials and methods

A polyamide-6 (PA6) extrusion grade (Akulon® K122) was supplied in pellet form by DSM, Geleen (The Netherlands). A sodium montmorillonite (MMT) Cloisite® Na^+ and a modified MMT Cloisite® 30B (C30B), supplied by Southern Clay Products, were used as nanofillers. C30B is a natural MMT modified with a methyl, tallow, bis-2-hydroxyethyl, quaternary ammonium. Layer spacing d_{001} before polymer incorporation is 1.85 nm. Two microcomposites filled with Cloisite® Na^+ (PANM2 and PANM5) and two nanocomposites filled with C30B (PAC2 and PAC5) were prepared by melt compounding in a twin screw microextruder (Micro 15, DSM) at a speed of 100 rpm at 240°C for 5 min under nitrogen atmosphere. The numbers in sample denomination refer to clay weight fractions. All clay concentrations reported correspond to the amount of inorganic silicate filler, i.e., MMT, rather than organoclay, because the silicate is the reinforcing component. The virgin PA6 referred as PA0 underwent the same processing route without any clay.

The state of dispersion of the nanofillers was observed using a TEI Tecnai transmission electron microscope (TEM) operating at an accelerating voltage of 200 kV. Ultra-thin sections of specimens were obtained by cryogenic ultramicrotoming. Specimens for TEM analyses were prepared from compression-molded sheets that were used for modulus and dynamic mechanical analyses (DMA) testing. It is, thus, ensured that the specimens for mechanical measurements and TEM have the same clay orientation and clay aspect ratio. To extract relevant morphological data from TEM pictures, one must be very careful, because a lot of errors can be made. A TEM section should be much thinner than the dimension of the smallest particle in the sample, to prevent overlapping of particles at different depths of the sample. For nanocomposites, this requirement cannot be met. This makes it very difficult to determine correctly the amount of clay or the distance between platelets.

The extruded PA6 and its nanocomposite pellets were compression molded into specimens, for Young's modulus (with a dimension of $75 \times 4 \times 1$ mm^3) and DMA ($45 \times 5 \times 1$ mm^3) measurements, at a temperature of 245°C under a pressure of 100 bar. Before extruding and compression molding, the pellets were dried under vacuum at 80°C for at least 12 h to avoid moisture induced degradation reactions. Using an Instron testing device, tensile tests were achieved at room temperature and under a constant strain rate of 0.001 s^{-1}. DMA tests were performed under torsional mode on a rheometrics ARES (TA Instruments). Samples were subjected to a sinusoidal strain at a frequency of 1 Hz, a static strain of 0.3% and a strain amplitude of 0.2%. The storage and loss modulus curves were recorded from −40°C to 120°C.

A Perkin-Elmer Diamond differential scanning calorimetry (DSC) was used to investigate the crystallization behavior. About 7 mg of the extruded pellets were heated to 280°C and held at 280°C for 10 min to eliminate the influence of thermal history, then cooled at a rate of 10°C/min down to 25°C.

The experimental results are outlined in the next section.

Experimental results

An indication of nanofiller dispersion achieved in PAC and PANM nanocomposites is provided in the TEM images of Figures 1 and 2. It can be seen that the PAC nanocomposites exhibit better nanofiller dispersion than the PANM nanocomposites. PAC and PANM nanocomposites exhibit exfoliated and intercalated structures, respectively. As shown in Figure 1, individual clay platelets, appearing as straight or slightly curved dark lines, are well dispersed in the PAC nanocomposites. Note that exfoliation is noticed for the two clay loadings. Some tactoids may also be seen. In the micrograph of Figure 2(a), a general view of the nanofiller dispersion in the PANM2 nanocomposite is shown. Only clay tactoids of different sizes are observed. The layered structure of clay can be distinctly identified in the high-magnification micrograph of Figure 2(b). Functionalization, used for the organophilization of the clay, significantly improves the state of dispersion. Indeed, it leads to an increased number of clay platelets individually dispersed in the matrix and, consequently, should lead to an increased volume fraction of constrained region around nanofillers. Moreover, the aspect ratio of fillers achieved in an exfoliated state is smaller. Thus, we expect increased mechanical properties for the PAC nanocomposites compared with the PANM nanocomposites.

DMA results are shown in Figure 3 for PA0 in comparison with the nanocomposites. The addition of MMT modifies the response of the polymer but modulus enhancement differs according to the type of nanocomposite. It can be seen that magnitude of the storage modulus significantly changes for the

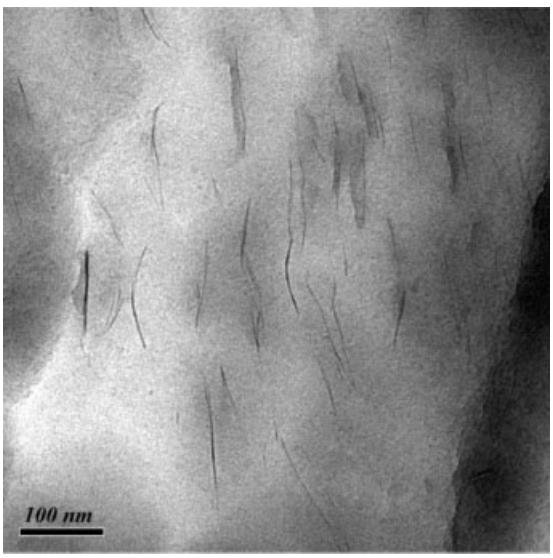

Figure 1 TEM micrograph of PAC2 nanocomposite.

PAC nanocomposites. The increase in storage modulus is less pronounced for the PANM nanocomposites. The reinforcement is thus larger in the exfoliated systems than in the intercalated systems and it increases with MMT content. As compared with PA0, the temperature of the main relaxation α is shifted toward higher temperatures for PAC nanocomposites.

The mechanical properties of nanocomposites depend on the properties of both polymer matrix and mineral phase. In a nanocomposite, the contact area between polymer and reinforcements is extremely magnified. It is, therefore, expected that polymer properties inside the nanocomposite are different from those of the unfilled polymer. Let us now discuss how the crystalline structure of the polymer phase in polymer/clay nanocomposites is changed by the presence of clay platelets. PA6 is a semi-crystalline polymer with a high melting

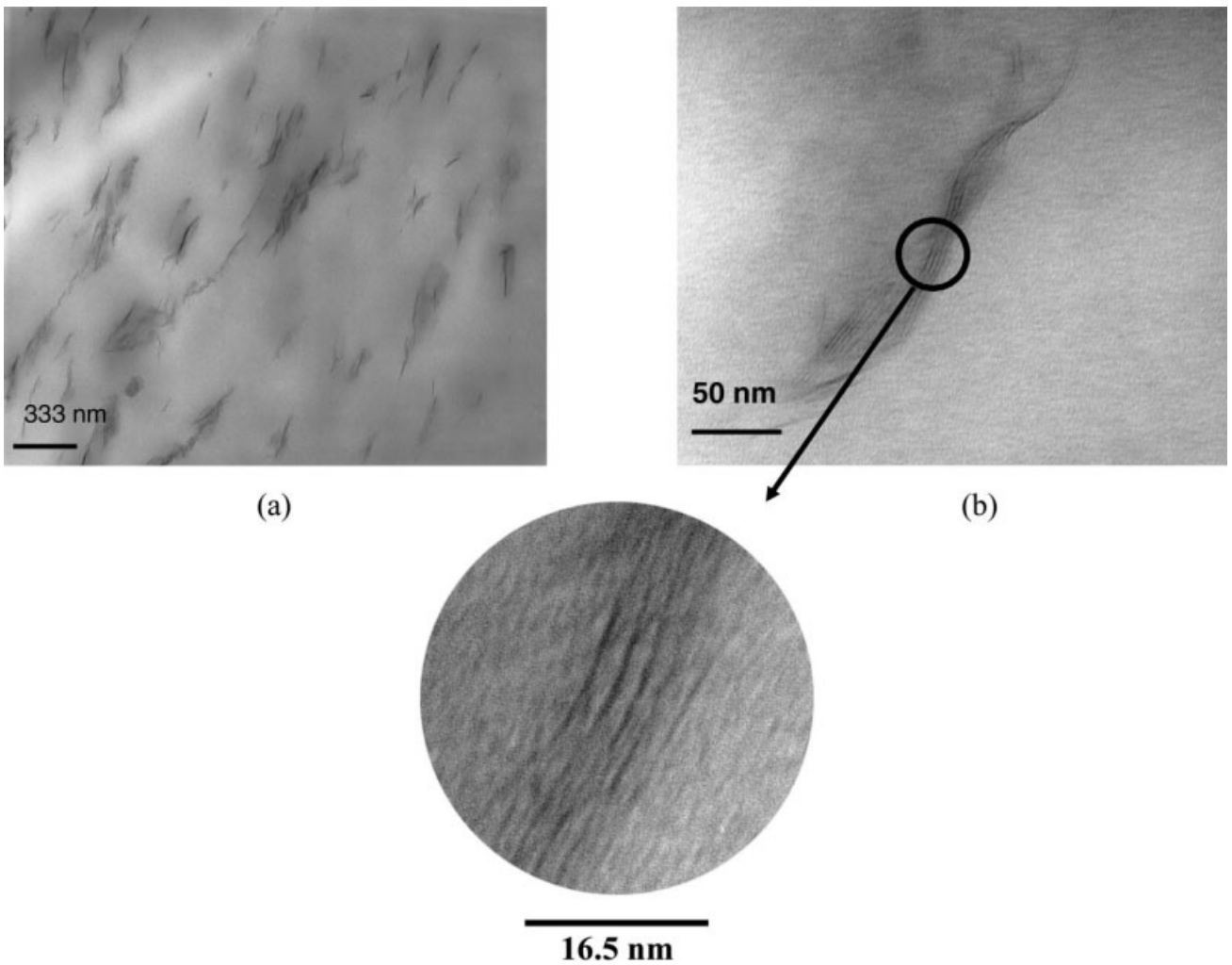

Figure 2 (a) TEM micrograph of PANM2 nanocomposite and (b) high-magnification micrograph revealing well-intercalated clay layers.

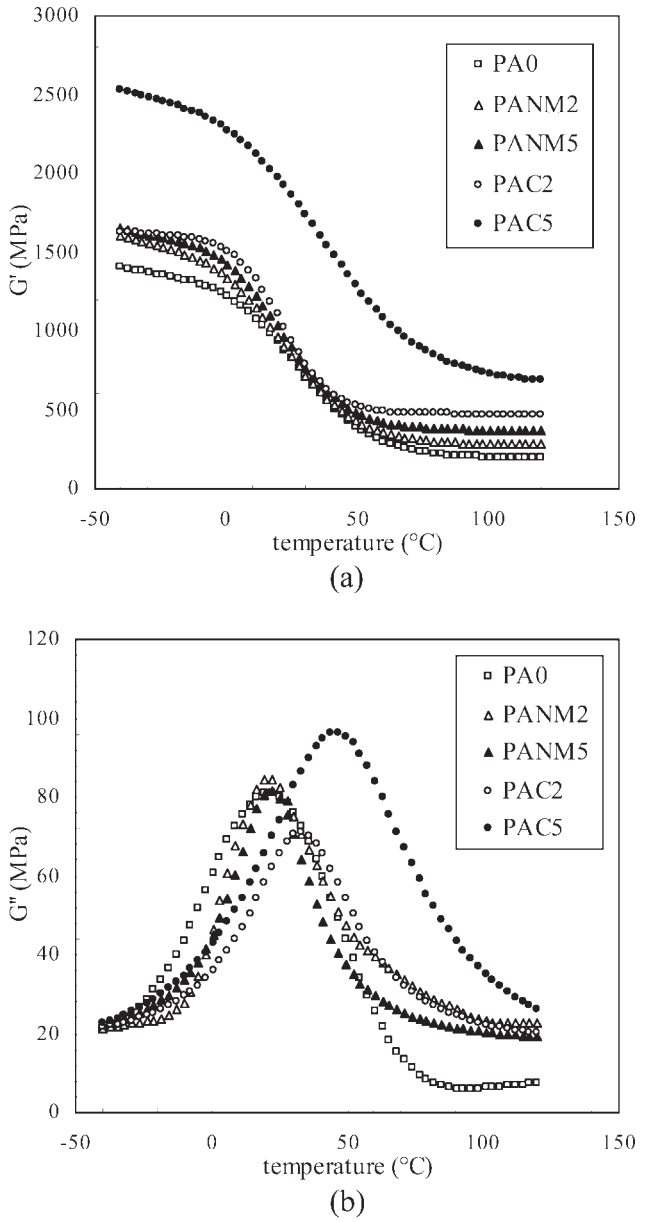

Figure 3 DMA results: (a) storage and (b) loss modulus with temperature.

temperature. This is caused by the hydrogen bonds that provide strong attractive forces between neighboring chains. PA6 can crystallize in the α-, β-, or γ-crystal forms, depending on environmental conditions. Under slow cooling, PA6 crystallizes in the α-form and under fast cooling in the β-crystal structure. Generally, the γ-crystal phase is obtained under extensional stress during fiber spinning or by addition of chemicals that change the nature of the hydrogen bonds. In the work at Toyota Research,[1,2] it was shown that the γ-form is also present in the case of PA6/clay nanocomposites. It is a consequence of the bond between amine end groups and the clay surface. This inhibits the α-crystalline structure and forms the γ-crystalline structure by default.

In a polymer/clay nanocomposite, the distance between clay platelets is extremely small. It can be expected that not only the crystalline structure but also crystallisation and melting kinetics are severely modified by the presence of the clay platelets. Clay was found to accelerate crystallisation in PA6. Kojima et al.[2] showed that the clay layers determine the orientation of PA6 chains in PA6/clay nanocomposites. The crystal weight fraction, obtained from DSC measurements, is presented in Figure 4. The values of crystal weight fraction were calculated using a melting enthalpy of 230 J/g for 100% crystalline PA[27] (the filler weight fraction contribution being subtracted). The presence of the silicate has little influence on the degree of crystallinity of the semi-crystalline polymer matrix.

Figure 4 depicts also the area under the loss modulus–temperature curve for PA0 and its nanocomposites. The increase in the dissipated energy for PAC nanocomposites, when compared with that of PANM nanocomposites, confirms better interaction between the functionalized nanofillers and the polymer. These data suggest a morphological difference in the amount of constrained region. The fraction of constrained region was estimated from the approach presented by Kojima et al.[2] It is expressed as

$$\phi^I = 1 - \frac{W}{W_0}\left(1 - \phi_0^I\right) \tag{1}$$

where ϕ_0^I is the crystal fraction of PA0 and W is the energy loss fraction defined by

$$W = \frac{\pi G''}{\pi G'' + G'} \tag{2}$$

in which G' is the storage modulus and G'' is the loss modulus. In eq. (1), W_0 is the energy loss referring to PA0.

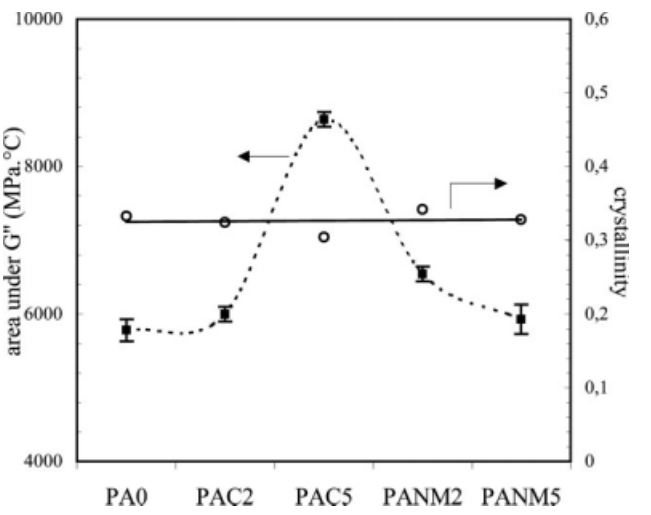

Figure 4 Area under the loss modulus–temperature curve and crystallinity for PA0 and its nanocomposites.

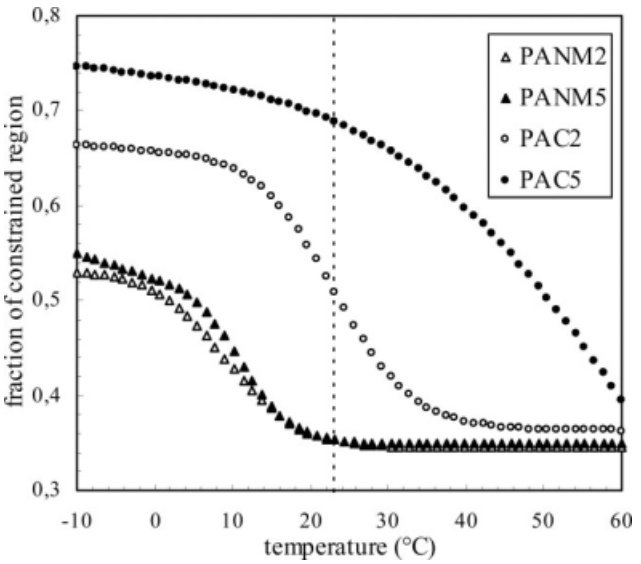

Figure 5 Fraction of constrained region with temperature.

Figure 5 presents the fraction of constrained region for PAC and PANM nanocomposites. The evolution of the fraction of constrained region with temperature has a sigmoidal shape. The relation of clay dispersion to the amount of constrained region can be clearly observed. In the case of PAC nanocomposites, the fraction of constrained region increases with an increase in clay content, whereas it remains nearly constant in the case of PANM nanocomposites. In all cases, the constrained region constitutes a large fraction of the polymer matrix.

The results of tensile tests in terms of overall elastic modulus are summarized in Table I. For each clay weight fraction, 15 tests were performed. The stiffness monotonically increases with filler content. PAC nanocomposites exhibit higher level of elastic modulus enhancement than PANM nanocomposites. Poor dispersion of clay platelets is shown to correlate with lower stiffness. The further stiffness enhancement for the PAC nanocomposites can be attributed to a combination of a better dispersion of the clay platelets and an increased extent of the constrained region.

MODELING

Micromechanical analytical modeling

In the present section, a micromechanical model for unidirectionally and randomly oriented discrete elastic isotropic spheroids randomly dispersed in a continuous elastic isotropic medium is presented. The continuous medium is the polymer matrix. The aspect ratio α of the spheroid is defined as the ratio between the length of the major axis 2′ and the length of the minor axis 1′ (Fig. 6). The lengths of the axes 2′ and 1′ are, respectively, the thickness and the length of the particle. In this case, the spheroid becomes a disk. The hierarchical morphology of the nanocomposite is taken into account according to an equivalent stiffness method[9,11,13] presented in Figure 6. The clay particle is a layered structure consisting of several parallel clay sheets separated by matrix, i.e., a laminate-like structure. In the hierarchical methodology, the silicate stacks are replaced by homogeneous particles with constructed equivalent anisotropic stiffness. The constrained region, which may be seen as an interphase between the reinforcement and the bulk matrix due to local matrix–particle interaction, is explicitly taken into account. It is assumed to have the same aspect ratio as the clay platelet. A three-phase composite (comprising particles, interphases, and polymer matrix) is then considered. Interfaces between the three phases are assumed to be perfectly bonded.

In the following derivation, the bold-face letters represent tensors. The dot represents the tensor multiplication between two fourth-order tensors, whereas the double dot denotes the tensor contraction between a fourth-order tensor and a second-order tensor. The letters *M*, *P*, and *I* are used to denote the matrix, the particle, and the interphase, respectively.

Stiffness analytical formulation for exfoliated nanocomposites

Unidirectionally oriented particles

The local heterogeneous stress field is derived according to the equivalent inclusion method and eigenstrain concept.[28] It may be expressed as follows:

$$\boldsymbol{\sigma}(\mathbf{x}) = \begin{cases} \mathbf{C}^0 : (\boldsymbol{\varepsilon}_0 + \boldsymbol{\varepsilon}'(\mathbf{x})) & \mathbf{x} \in M \\ \mathbf{C}^P : (\boldsymbol{\varepsilon}_0 + \boldsymbol{\varepsilon}'(\mathbf{x})) & \mathbf{x} \in P \\ \mathbf{C}^I : (\boldsymbol{\varepsilon}_0 + \boldsymbol{\varepsilon}'(\mathbf{x})) & \mathbf{x} \in I \end{cases} \quad (3)$$

in which $\mathbf{C}^0$, $\mathbf{C}^P$, and $\mathbf{C}^I$ are the fourth-order stiffness tensors of the matrix, the particle, and the interphase, respectively, $\boldsymbol{\varepsilon}_0$ is the far-field strain and $\boldsymbol{\varepsilon}'(\mathbf{x})$ is the disturbance strain due to the presence of the heterogeneities.

TABLE I
Tensile Results: Overall Young's Modulus

Sample code	Weight fraction	E_{11} (GPa)
PA0	0	2.97 ± 0.03
PAC2	0.02	3.71 ± 0.03
PAC5	0.05	4.64 ± 0.04
PANM2	0.02	3.23 ± 0.03
PANM5	0.05	3.77 ± 0.07

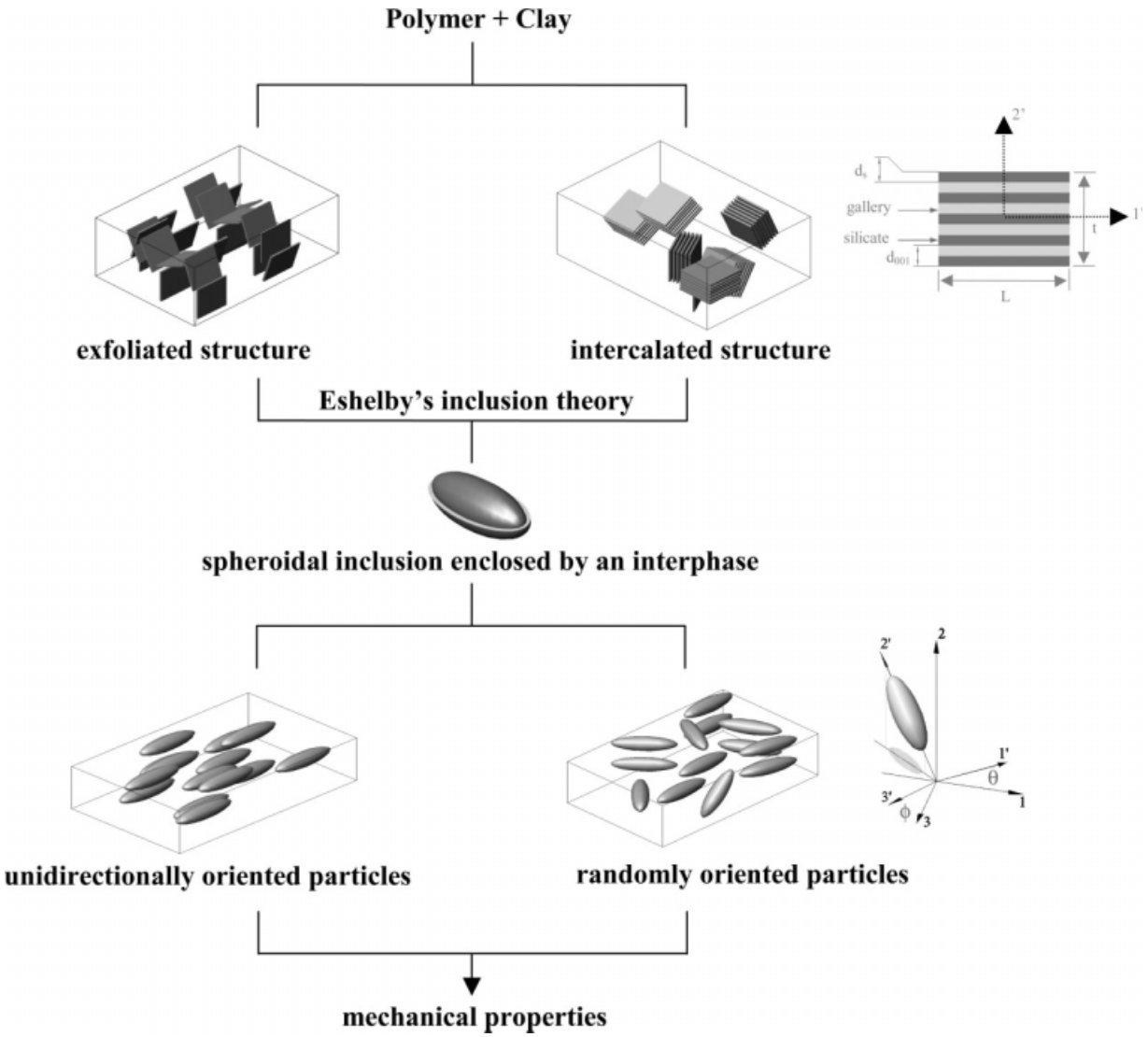

Figure 6 Schematic visualization of the equivalent stiffness method used to determine the mechanical properties of intercalated polymer/clay nanocomposites.

Considering the Eshelby concept of eigenstrain, the stress field of the homogeneous medium equivalent to the heterogeneous material may be established. Equation (3) can be rewritten as

$$\boldsymbol{\sigma}(\mathbf{x}) = \begin{cases} \mathbf{C}^0 : (\boldsymbol{\varepsilon}_0 + \boldsymbol{\varepsilon}'(\mathbf{x})) & \mathbf{x} \in M \\ \mathbf{C}^0 : (\boldsymbol{\varepsilon}_0 + \boldsymbol{\varepsilon}'(\mathbf{x}) + \boldsymbol{\varepsilon}_\mathbf{P}^*\mathbf{x}) & \mathbf{x} \in P \\ \mathbf{C}^0 : (\boldsymbol{\varepsilon}_0 + \boldsymbol{\varepsilon}'(\mathbf{x}) + \boldsymbol{\varepsilon}_\mathbf{I}^*(\mathbf{x})) & \mathbf{x} \in I \end{cases} \quad (4)$$

where $\boldsymbol{\varepsilon}_P^*$ and $\boldsymbol{\varepsilon}_I^*$ are the averaged eigenstrains inside the mediums P and I:

$$\boldsymbol{\varepsilon}_P^* = \mathbf{T}^P : \boldsymbol{\varepsilon}_0 \text{ and } \boldsymbol{\varepsilon}_I^* = \mathbf{T}^I : \boldsymbol{\varepsilon}_0 \quad (5)$$

The formulation of these eigenstrains is based on the double-inclusion method of Hori and Nemat-Nasser.[29] In eq. (5), $\mathbf{T}^P$ and $\mathbf{T}^I$ are two fourth-order tensors defined by

$$\mathbf{T}^P = -\left[(\mathbf{S}^P + \mathbf{A}^P) + \Delta\mathbf{S} \cdot \left(\mathbf{S}^P - \phi^{P/\Sigma}/\phi^{I/\Sigma}\Delta\mathbf{S} + \mathbf{A}^I\right)^{-1} \cdot \left(\mathbf{S}^P - \phi^{P/\Sigma}/\phi^{I/\Sigma}\Delta\mathbf{S} + \mathbf{A}^P\right)\right]^{-1} \quad (6)$$

and

$$\mathbf{T}^I = -\left[\Delta\mathbf{S} + (\mathbf{S}^P + \mathbf{A}^P) \cdot \left(\mathbf{S}^P - \phi^{P/\Sigma}/\phi^{I/\Sigma}\Delta\mathbf{S} + \mathbf{A}^P\right)^{-1} \cdot \left(\mathbf{S}^P - \phi^{P/\Sigma}/\phi^{I/\Sigma}\Delta\mathbf{S} + \mathbf{A}^I\right)\right]^{-1} \quad (7)$$

In relations (6) and (7), $\phi^{P/\Sigma}$ and $\phi^{I/\Sigma}$ denote the particle and interphase volume fraction inside the medium $\Sigma = P + I$, $\Delta\mathbf{S}$ defines the difference $\mathbf{S}^\Sigma - \mathbf{S}^P$ where $\mathbf{S}^\Sigma$ and $\mathbf{S}^P$ are the Eshelby tensors for the entire inclusion medium Σ and the particle

medium P, respectively. These tensors only depend on the aspect ratio of the medium and on the Poisson's ratio of the matrix. The components of Eshelby tensor are given in Appendix A. Because it is assumed that the interphase around the particle has the same aspect ratio as that of the particle: $\mathbf{S}^{\Sigma} = \mathbf{S}^{P} = \mathbf{S}$ and $\Delta\mathbf{S} = 0$. Equations (6) and (7) can be rewritten as

$$\mathbf{T}^{P} = -\left(\mathbf{S} + \mathbf{A}^{P}\right)^{-1} \text{ and } \mathbf{T}^{I} = -\left(\mathbf{S} + \mathbf{A}^{I}\right)^{-1} \quad (8)$$

where $\mathbf{A}^{P}$ and $\mathbf{A}^{I}$ are two fourth-order tensors expressed by

$$\mathbf{A}^{P} = \left(\mathbf{C}^{P} - \mathbf{C}^{0}\right)^{-1} \cdot \mathbf{C}^{0} \text{ and } \mathbf{A}^{I} = \left(\mathbf{C}^{I} - \mathbf{C}^{0}\right)^{-1} \cdot \mathbf{C}^{0} \quad (9)$$

The eigenstrain $\boldsymbol{\varepsilon}^{*}$ for the entire inclusion medium $\boldsymbol{\Sigma}$ (including particles and interphases) can be written as

$$\boldsymbol{\varepsilon}^{*} = \mathbf{T}^{\Sigma} : \boldsymbol{\varepsilon}_{0} \quad (10)$$

In eq. (10), $\mathbf{T}^{\Sigma}$ is the fourth-order tensor given by the following formula:

$$\mathbf{T}^{\Sigma} = \phi^{P/\Sigma}\mathbf{T}^{P} + \phi^{I/\Sigma}\mathbf{T}^{I} \quad (11)$$

Ju and Chen[30] derived the general governing equations for composites containing unidirectionally oriented particles. In the case of three-phase nanocomposites, and according to Liu and Sun,[31] one may write

$$\begin{aligned} \boldsymbol{\sigma} &= \mathbf{C} : \boldsymbol{\varepsilon} = \mathbf{C}^{0} : \left(\boldsymbol{\varepsilon} - \phi^{\Sigma}\boldsymbol{\varepsilon}^{*}\right) \\ \boldsymbol{\varepsilon} &= \boldsymbol{\varepsilon}_{0} + \phi^{\Sigma}\mathbf{S} : \boldsymbol{\varepsilon}^{*} = \left(\mathbf{I} + \phi^{\Sigma}\mathbf{S} : \mathbf{T}^{\Sigma}\right) : \boldsymbol{\varepsilon}_{0} \end{aligned} \quad (12)$$

In eq. (12), ϕ^{Σ} defines the volume fraction of the entire inclusion medium Σ.

Considering eqs. (10) and (12), the stiffness tensor of the nanocomposite is then given by

$$\mathbf{C} = \mathbf{C}^{0} \cdot \left[\mathbf{I} - \phi^{\Sigma}\mathbf{T}^{\Sigma} \cdot \left(\phi^{\Sigma}\mathbf{S} \cdot \mathbf{T}^{\Sigma} + \mathbf{I}\right)^{-1}\right] \quad (13)$$

where $\mathbf{I}$ is the fourth-order identity tensor.

Randomly oriented particles

A three-dimensional random particle orientation is now considered. The local and global coordinates are defined in Figure 6. The primed coordinate system (1′, 2′, 3′) corresponds to local axes and the unprimed coordinate system (1, 2, 3) to global axes. When all reinforcements are randomly oriented in the three-dimensional space, the averaging process over all orientations can be performed. The stiffness tensor of the nanocomposite can be given by

$$\left\langle C_{ijkl} \right\rangle = \int_{0}^{\pi}\int_{0}^{\pi} Q_{mi}Q_{nj}C_{mnpq}Q_{pk}Q_{ql}P(\theta, \phi)\sin\theta d\theta d\phi \quad (14)$$

where $P(\theta,\phi)$ is the probability density function. Assuming a uniform random distribution, this function is equal to $1/2\pi$.

In eq. (14), Q_{ij} is the transformation matrix:

$$Q_{ij} = \begin{bmatrix} \cos\theta & \sin\theta\cos\phi & \sin\theta\sin\phi \\ -\sin\theta & \cos\theta\cos\phi & \cos\theta\sin\phi \\ 0 & -\sin\phi & \cos\phi \end{bmatrix} \quad (15)$$

where θ represents the angle between 1 and 1′, and ϕ the angle between 3 and 3′.

Stiffness analytical formulation for intercalated nanocomposites

The same equations as developed above are used, replacing the silicate stacks by an equivalent particle. The structure of intercalated silicate stacks is schematically shown in Figure 6. It can be seen as a laminated composite, consisting of several platelets separated by polymer chains, embedded in the matrix material. To deal with this peculiar particle morphology, the hierarchical approach[9,11,13] is introduced in the model. It relies on clay structural parameters, including the average interlayer spacing d_{001} and the average number of silicate layers N in the intercalated structure. This approach leads to an estimate of the geometry and mechanical properties of the equivalent clay particle. The particle thickness t can be expressed as

$$t = (N-1)d_{001} + d_{s} \quad (16)$$

d_s being the silicate layer thickness.

The silicate as well as the confined polymer matrix (so-called gallery layer) in the intersilicate layers are assumed to be isotropic. The overall elastic properties of the equivalent particle may be expressed, according to Tsai and Hahn,[32] as follows:

$$E_{P,11} = E_{P,33} = \chi E_{\text{silicate}} + (1-\chi)E_{\text{gallery}} \quad (17)$$

$$E_{P,22} = \frac{E_{\text{silicate}}E_{\text{gallery}}}{\chi E_{\text{gallery}} + (1-\chi)E_{\text{silicate}} - \chi(1-\chi)\eta_{1}E_{\text{gallery}}E_{\text{silicate}}} \quad (18)$$

$$\nu_{P,12} = \nu_{P,32} = \chi\nu_{\text{silicate}} + (1-\chi)\nu_{\text{gallery}} \quad (19)$$

$$\nu_{P,13} = \frac{\nu_{\text{silicate}}\chi E_{\text{silicate}}\left(1-\nu_{\text{gallery}}^{2}\right) + \nu_{\text{gallery}}(1-\chi)E_{\text{gallery}}\left(1-\nu_{\text{silicate}}^{2}\right)}{\chi E_{\text{silicate}}\left(1-\nu_{\text{gallery}}^{2}\right) + \nu_{\text{gallery}}(1-\chi)E_{\text{gallery}}\left(1-\nu_{\text{silicate}}^{2}\right)} \quad (20)$$

$$G_{P,12} = G_{P,32} = \frac{G_{\text{silicate}} G_{\text{gallery}}}{\chi G_{\text{gallery}} + (1-\chi) G_{\text{silicate}} - \chi(1-\chi)\eta_2 G_{\text{gallery}} G_{\text{silicate}}} \quad (21)$$

$$G_{P,13} = \frac{E_{P,11}}{2(1+\nu_{P,13})} \quad (22)$$

In relations (17)–(21), χ is the silicate volume fraction in the equivalent particle:

$$\chi = \frac{V_{\text{silicate}}}{V_P} = \frac{N d_s}{t} \quad (23)$$

where V_{silicate} is the volume of silicate in the equivalent particle and V_P the volume of the equivalent particle. Parameters η_1 and η_2 in eqs. (18) and (21) are given in Appendix B.

This estimate of the idealized homogeneous particle is introduced into the micromechanical analytical model and it requires eight input parameters: the Young's moduli E_{silicate}, E_{gallery}, the Poisson's ratios ν_{silicate} and ν_{gallery}, and the clay structural parameters L, N, d_{001}, and d_s.

Because the characteristics of nanocomposites are known in terms of silicate weight fraction, it is necessary to express the particle volume fraction as function of the silicate weight fraction (the developments are given in Appendix C).

Particle size effect

The interphase thickness can be seen as a characteristic length scale for nanocomposites. Therefore, in addition to the particle shape effect, the particle size effect can be explicitly introduced in the model. The interphase volume fraction inside Σ can be expressed in terms of the particle volume fraction inside Σ and some geometrical parameters

$$\phi^{I/\Sigma} = \phi^{P/\Sigma}\left[\left(1+\frac{2e}{t}\right)^2\left(1+\frac{2e}{L}\right) - 1\right] \quad (24)$$

where t and L are the thickness and length of the particle, respectively, and e is the thickness of the interphase.

Interphase elastic properties

Moreover, because the interphase is assumed heterogeneous, it is taken as a multilayered region to account for the interphase properties gradient. The inhomogeneous interphase is divided into n homogeneous layers and the fourth-order tensor of relation (11) is rewritten as

$$\mathbf{T}^{\Sigma} = \phi^{P/\Sigma}\mathbf{T}^{P} + \sum_{i=1}^{n} \phi_i^{I/\Sigma}\mathbf{T}_i^{I} \quad (25)$$

where $\phi_i^{I/\Sigma}$ is the volume fraction of the layer i inside Σ and $\mathbf{T}_i^I$ is the fourth-order tensor given by

$$\mathbf{T}_i^I = -\left(\mathbf{S} + \mathbf{A}_i^I\right)^{-1} \quad (26)$$

in which the fourth-order mismatch tensor $\mathbf{A}_i^I$ of the layer i is now expressed as

$$\mathbf{A}_i^I = \left(\mathbf{C}_i^I - \mathbf{C}^0\right)^{-1} \cdot \mathbf{C}^0 \quad (27)$$

In the case of an exfoliated nanocomposite, the elastic modulus of the interphase is assumed to be governed by the following equation

$$(E_I)_i = \frac{t_\Sigma}{t_i}E_M + \left(\frac{t_\Sigma - t_i}{e}\right)\left(\gamma E_P - \frac{2t_\Sigma}{t}E_M\right) \quad (28)$$

where $t_\Sigma = t/2 + e$, $t_i \in [t/2, t_\Sigma]$ and γ is a material parameter controlling the stiffness of the first layer of the interphase. Note that the Poisson's ratio of the interphase is taken equal to that of the matrix. The boundary conditions of eq. (28) are given by

$$(E_I)_{i=1} = \gamma E_P \quad \text{for} \quad t_{i=1} = \frac{t}{2}$$

and

$$(E_I)_{i=N} = E_M \quad \text{for} \quad t_{i=N} = e \quad (29)$$

In the case of an intercalated nanocomposite, the interphase is no longer isotropic because the particles are anisotropic. The following governing equations are proposed:

$$\left(E_{I,11}\right)_i = \left(E_{I,33}\right)_i = \frac{t_\Sigma}{t_i}E_M + \left(\frac{t_\Sigma - t_i}{e}\right)\left(\gamma E_{P,11} - \frac{2t_\Sigma}{t}E_M\right) \quad (30)$$

$$\left(E_{I,22}\right)_i = E_M \quad (31)$$

$$\left(\nu_{I,12}\right)_i = \left(\nu_{I,32}\right)_i = \left(\nu_{I,13}\right)_i = \nu_M \quad (32)$$

$$\left(G_{I,12}\right)_i = \left(G_{I,32}\right)_i = G_M \quad (33)$$

$$\left(G_{I,13}\right)_i = \frac{\left(E_{I,11}\right)_i}{2(1+\nu_M)} \quad (34)$$

FE modeling

Because the stiffness of a nanocomposite with homogeneously distributed clay platelets is expected to be different from that of a nanocomposite with localized regions of clay platelets, an FE analysis taking this feature into account was achieved to provide an accurate prediction of the Young's modulus. The

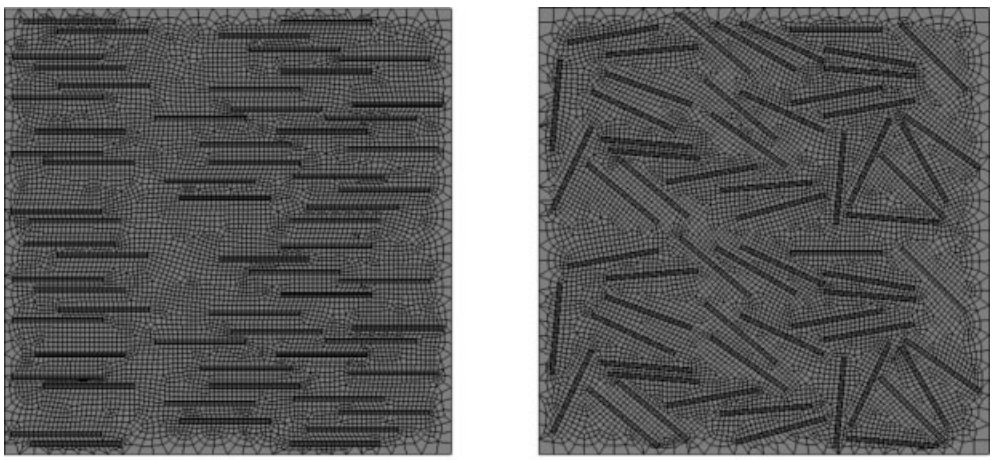

Figure 7 Mesh of RVE including (a) unidirectionally oriented particles and (b) randomly oriented particles.

simulations were performed using the FE software MSC.Marc© under two-dimensional plane strain conditions. Typical representative volume elements (RVE) used in the FE simulations are presented in Figure 7. The clay platelets were considered as rectangular-like particles with uniform length and thickness. The matrix, particles, and interphase were meshed with four-node quadrilateral elements. Perfect bonding was assumed for interfaces. The RVE was subjected to a small-strain axial tensile loading. Two cases were considered to model the nanocomposites: (i) unidirectionally oriented and randomly dispersed particles [Fig. 7(a)]; and (ii) randomly oriented and dispersed particles [Fig. 7(b)].

Modeling results

This section is subdivided in two parts. In the first part, the purpose is to achieve a parametric study to point out the influence of the key parameters. In particular, the micromechanical model predictions are compared with both an FE modeling and with experimental results extracted from the literature. In the second part, because some key parameters are not completely provided in the literature (i.e., particle dimensions, number of silicate layers per stack, interlayer spacing, interphase volume fraction), the model predictions are compared with our experimental data because the required parameters are available in this case.

Parametric study

The matrix material elastic properties are 3000 MPa and 0.4 for the Young's modulus and the Poisson's ratio, respectively, which are typical values for thermoplastic polymers in the glassy state. As noted by Wang and Pyrz,[17] the mechanical properties and the microstructural parameters, such as the length of the MMT silicate, are not really defined. In the literature, the Young's modulus assigned to MMT platelets varies between 140 and 178 GPa. Here, we have taken 178 GPa for the Young's modulus and 0.23 for the Poisson's ratio. If the thickness of a single MMT layer is known to be about 1 nm, its length is not a constant and varies between 100 and 500 nm depending on the authors.[17] The aspect ratio of the particles is taken equal to 1/200. Unless otherwise stated, these values will be used in the remaining of the study.

Effect of particle volume fraction

An FE analysis of the reinforcement effect on the overall stiffness of the nanocomposite was performed and results are compared with the analytical

TABLE II
Comparison Between Analytical and FE Predictions of E_{11}/E_M

Volume fraction	Analyt. - UD	FE - UD	V - UD	Analyt. - R	FE - R	V - R
0.02	1.2443	1.2283	0.0068	1.1371	1.1352	0.0104
0.05	1.5953	1.5953	0.0144	1.3335	1.3455	0.0055
0.10	2.1463	2.1459	0.0307	1.6405	1.7591	0.0093

UD, unidirectionally oriented particles; R, randomly oriented particles.

TABLE III
Comparison Between Analytical and FE Predictions of E_{11}/E_M Taking into Consideration the Interphase

Volume fraction	Analyt. - UD	FE - UD	*V* - UD	Analyt. - R	FE - R	*V* - R
0.02	1.2655	1.2503	0.0036	1.1505	1.1594	0.0229
0.05	1.6461	1.6238	0.0116	1.3655	1.3624	0.0393
0.10	2.2416	2.2443	0.0333	1.6999	1.7925	0.0385

UD, unidirectionally oriented particles; R, randomly oriented particles.

model predictions. The FE simulation results are compared with the analytical predictions in Table II in the case of exfoliated morphologies. The two kinds of solutions provide similar results. Each FE value is averaged over 10 random distributions of particles in the RVE. The scatter of FE results is indicated by the variation factor *V* defined as the ratio of the standard deviation to the average value. The variation factor increases with increasing volume fraction when aligned particle nanocomposite is concerned. This can be attributed to the effect of particle interaction. For nanocomposites with randomly oriented particles, FE results slightly overestimate the analytical results with increasing volume fraction. This can be explained by the averaging process. Indeed, integration is taken for all orientations in the analytical model, whereas in the FE simulation, the result is obtained with a finite number of orientations. Moreover, the analytical model neglects the particle–particle interaction. RVE with interphase were also constructed. The interphase was assumed to be homogeneous and isotropic. Because no mechanical data are available for the interphase, a Young's modulus of $5 \times E_M$ and a Poisson's ratio of 0.4 were arbitrarily assigned. The volume fraction of the interphase inside the entire inclusion medium was fixed to 0.25. The FE simulation results and analytical predictions are shown in Table III. A good agreement is pointed out between the two kinds of solutions.

The analytical predictions are compared with the experimental data reported in literature[33,34] in Figure 8. These nanocomposites are made of MMT silicate dispersed in different polymer matrices. They are claimed to be fully exfoliated. The analytical predictions considering unidirectionally oriented particles in the composites overestimate the experimental data. Only the predictions of composites with randomly oriented particles provide reasonable estimates. The predictions are in very good agreement at low volume fractions but when the volume fraction becomes larger, the predictions somewhat underestimate the experimental data. Because uncertainties exist in the aspect ratio and the Young's modulus of the silicate, the analytical predictions may be considered as relatively good. However, this comparison can also reinforce the idea of the existence of a significant interphase in which the polymer stiffness has been altered by the interaction with the clay platelets. It could further suggest that the interphase has increased stiffness.

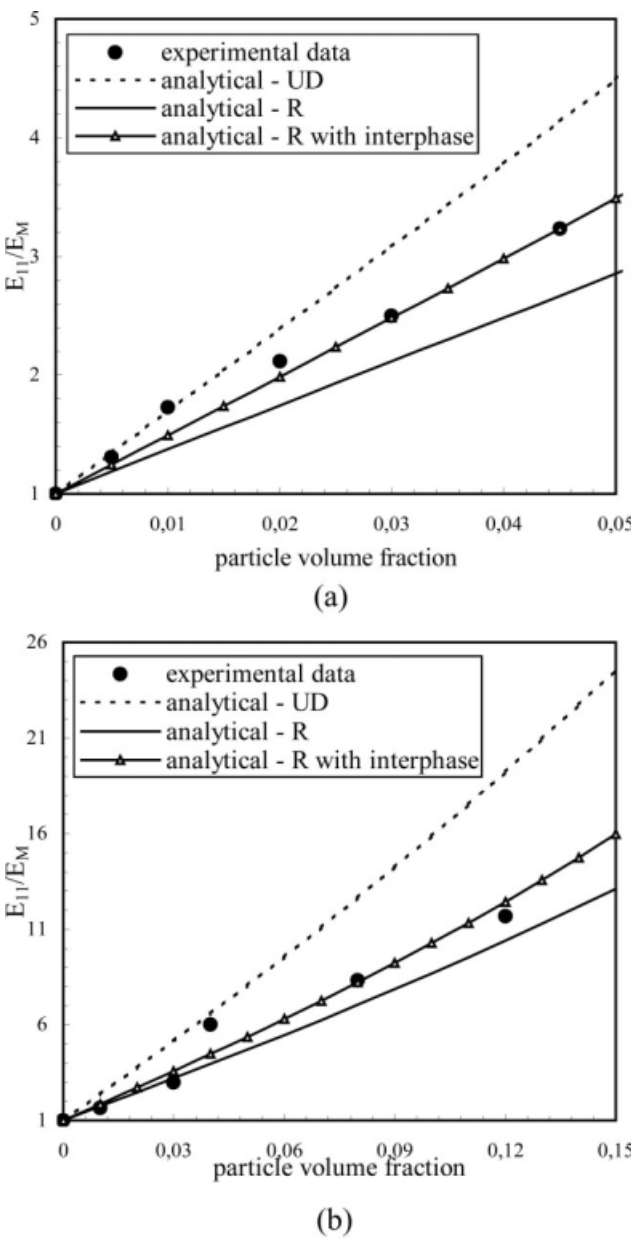

Figure 8 Comparison between analytical predictions and experimental data of the overall Young's modulus of (a) polyimide/clay nanocomposites[33] and (b) epoxy (in rubbery state)/clay nanocomposites[34] (UD, unidirectionally oriented particles; R, randomly oriented particles).

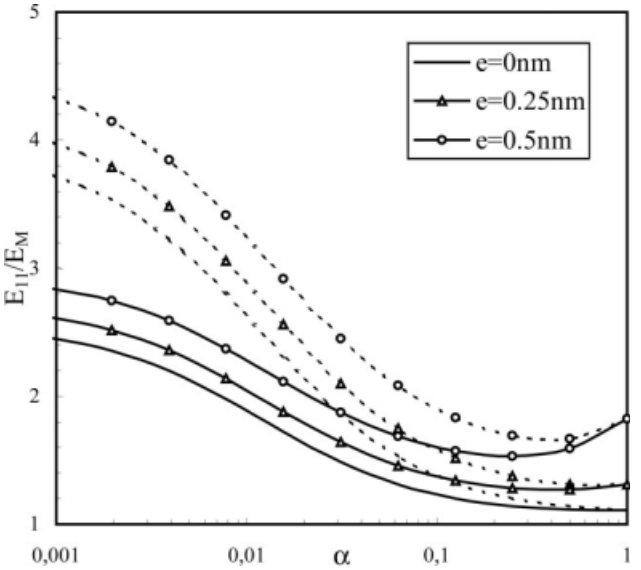

Figure 9 Effect of particle aspect ratio and interphase thickness on the overall Young's modulus (discontinuous lines: unidirectionally oriented particles, continuous lines: randomly oriented particles).

Effect of particle aspect ratio and particle size

As shown in Figure 8, the predictions are in very good agreement with the experimental data when considering the presence of the interphase and the particle size effect. The interphase thickness was fixed to 0.5 nm whatever the particle volume fraction. Moreover, the interphase was assumed to be homogeneous with a stiffness of $8 \times E_M$ and a Poisson's ratio of 0.4.

Figure 9 highlights the effect of particle aspect ratio and interphase thickness on the overall Young's modulus of the composite when considering the size effect. Two cases are considered: unidirectionally oriented particles and randomly oriented particles. The influence of particle orientation on the stiffness enhancement is clearly highlighted. It is shown that the smaller the aspect ratio is, the higher is the orientation effect. In the two cases, for the spherical particles (i.e., aspect ratio being equal to 1), the predictions give a lower bound. The degree of improvement highly depends on the aspect ratio. It is shown for a given interphase thickness that the smaller the aspect ratio is, the higher is the stiffness. The thickness and length of a silicate platelet are typically 1 nm and 200 nm, respectively, for MMT giving an aspect ratio of about 0.005. Therefore, as pointed out by other works in the literature,[10,11,15] platelets are the most efficient reinforcements among other types.

The effect of particle length and interphase thickness on the elastic modulus is illustrated in Figure 10. For a given interphase thickness, the effect of particle size may be clearly seen. The smaller the particle length is, the higher is the composite stiffness. However, at the micrometer scale, the particle size effect vanishes. With the presence of a constrained region, the elastic modulus of nanocomposites is higher than that of microcomposites.

Effect of inhomogeneous interphase

Let us now focus on the inhomogeneous nature of the interphase. The inhomogeneous interphase is approximated as 500 different homogeneous layers. The influence of γ parameter on the overall Young's modulus is presented in Figure 11(a) for unidirectionally and randomly oriented particles. The variation of the stiffness in the interphase is presented in Figure 11(b).

In the analysis presented above, only the exfoliated state was treated. The remainder of the parametric study introduces the equivalent stiffness method to deal with the intercalated layered state.

Effect of number of silicate layers and interlayer spacing

The effect of clay structural parameters on the overall Young's modulus of the nanocomposite is investigated. Each parameter is varied independently while keeping the others constant. The mechanical properties of the intercalated matrix are probably different from those of the bulk matrix material. A Young's modulus and a Poisson's ratio equal to those of the matrix were assigned to the gallery layer.

As shown in Figure 12, the number of silicate layers N per stack has a strong influence on the overall Young's modulus. An interlayer spacing d_{001}

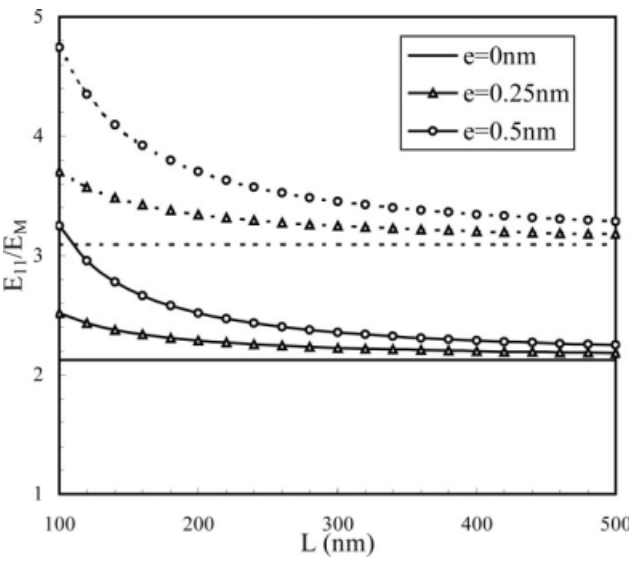

Figure 10 Effect of particle length and interphase thickness on the overall Young's modulus (discontinuous lines: unidirectionally oriented particles, continuous lines: randomly oriented particles).

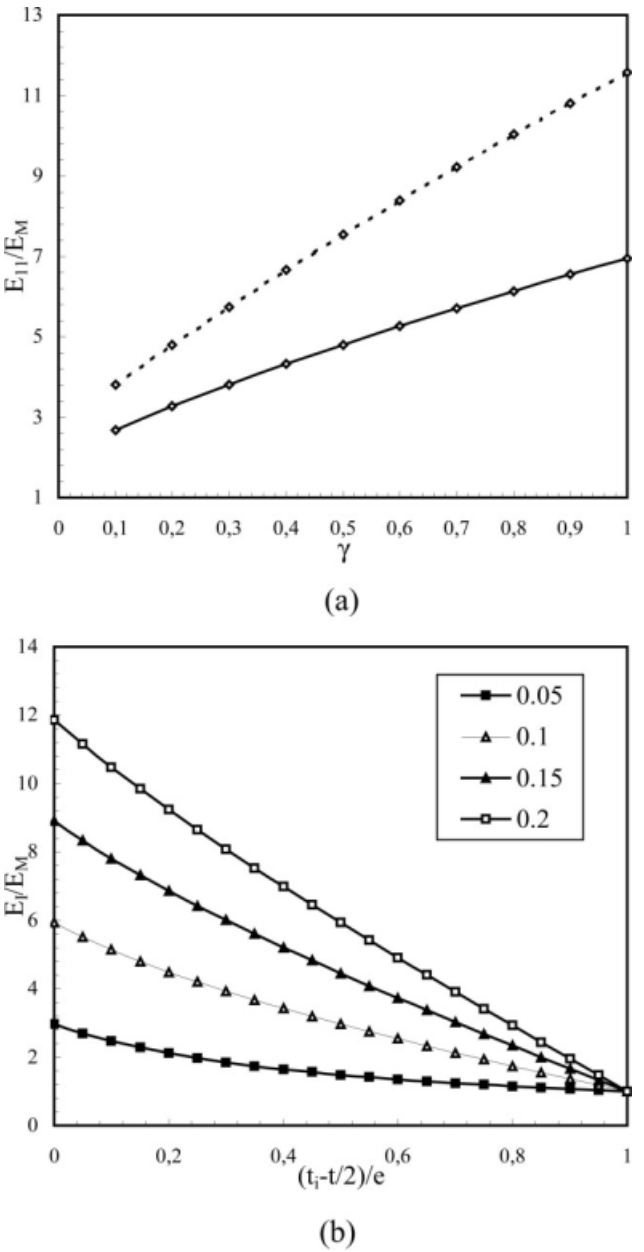

Figure 11 Effect of γ parameter on (a) the overall Young's modulus (discontinuous lines: unidirectionally oriented particles, continuous lines: randomly oriented particles) and (b) the variation of the stiffness in the interphase.

of 3 nm was taken. The effect of the Young's modulus of the matrix is clearly pointed out. A Young's modulus of 3000 MPa corresponds to a glassy polymer, whereas 1 MPa corresponds to a rubbery polymer. The higher the mismatch in modulus between the clay and the matrix is, the higher is the nanocomposite stiffness enhancement. This is consistent with the experimental data of Figure 8 where epoxy matrix in the rubbery state shows more pronounced stiffness enhancement than the matrix in the rigid state. The increase in N leads to a considerable decrease in the overall Young's modulus. Indeed, as highlighted in Figure 13(a), when N increases, the aspect ratio and the modulus of the equivalent particle, respectively, increases and decreases. Moreover, the decrease of the overall Young's modulus due to the transition from exfoliated state ($N = 1$) to intercalated state ($N \geq 2$) is less marked in the case of randomly oriented particles.

As depicted in Figure 14, lower nanocomposite modulus is obtained when increasing the interlayer spacing d_{001} (a value of 5 was attributed to N). However, the influence of d_{001} is weaker than that of N. The influence of the matrix stiffness is also

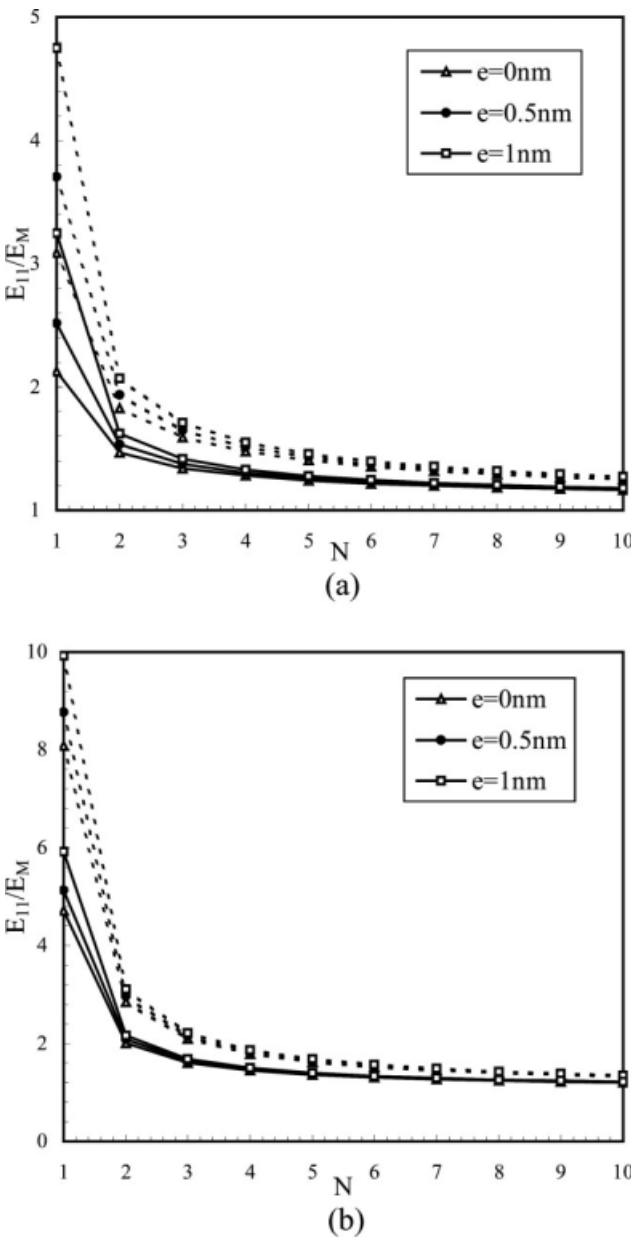

Figure 12 Effect of number of silicate layers on the overall Young's modulus (discontinuous lines: unidirectionally oriented particles, continuous lines: randomly oriented particles): (a) $E_M = 3000$ MPa, (b) $E_M = 1$ MPa.

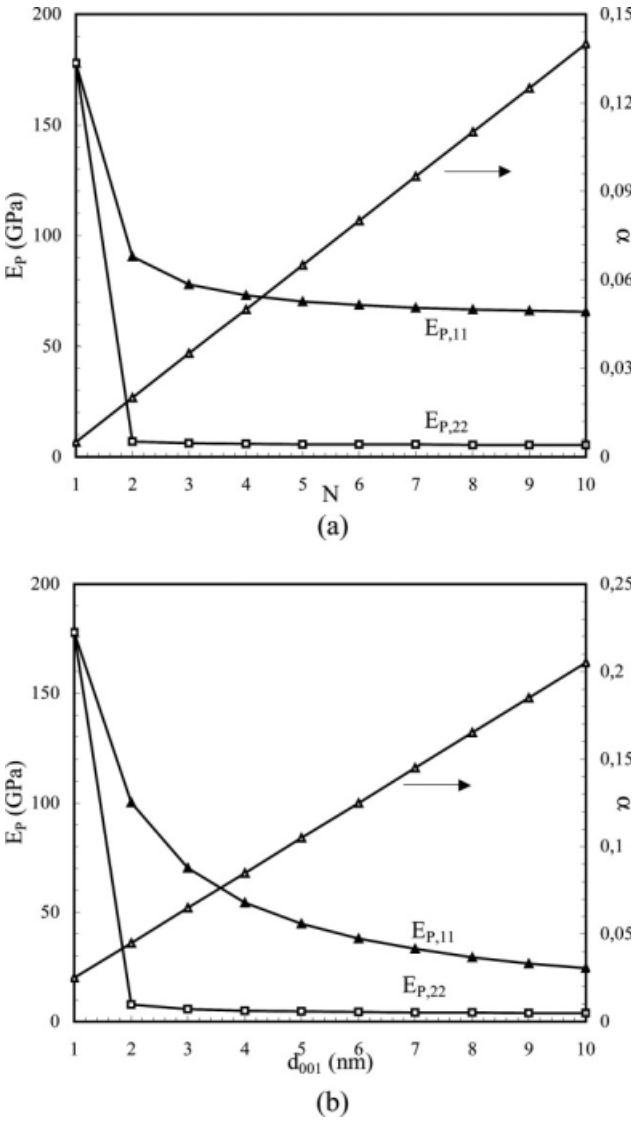

Figure 13 Young's modulus and aspect ratio of the particles versus (a) number of silicate layers and (b) interlayer spacing.

highlighted. The effect of d_{001} on the modulus of the equivalent particle is shown in Figure 13(b). The anisotropy of the intercalated silicate stack is reduced when d_{001} increases. Moreover, its transverse modulus is slightly affected by d_{001}.

Comparison with experimental data obtained on PA6 nanocomposites

As mentioned earlier, several inputs related to the structure of the nanocomposite are required by the modeling.

TEM micrographs show that the nanocomposites produced using Cloisite 30B exhibit exfoliated structures, whereas untreated clay (Cloisite Na^+) leads to intercalated structures. Functionalization used for the organophilization of the clay yields stronger interactions between the clay particles and the matrix, which results in better dispersion of the clay platelets. As a result, the PAC nanocomposites exhibit higher modulus enhancement compared with the PANM nanocomposites (Table I).

The length of silicate platelets L, estimated from TEM micrographs, was fixed to 150 nm. The thickness of silicate platelets d_s was taken equal to 1 nm. The number of silicate layers per stack N and the interlayer spacing d_{001} in the PAC nanocomposites were estimated from TEM micrographs [Fig. 2(b)]. An appreciable interlayer spacing of 2.5 nm was measured in the intercalated cluster. Note that this

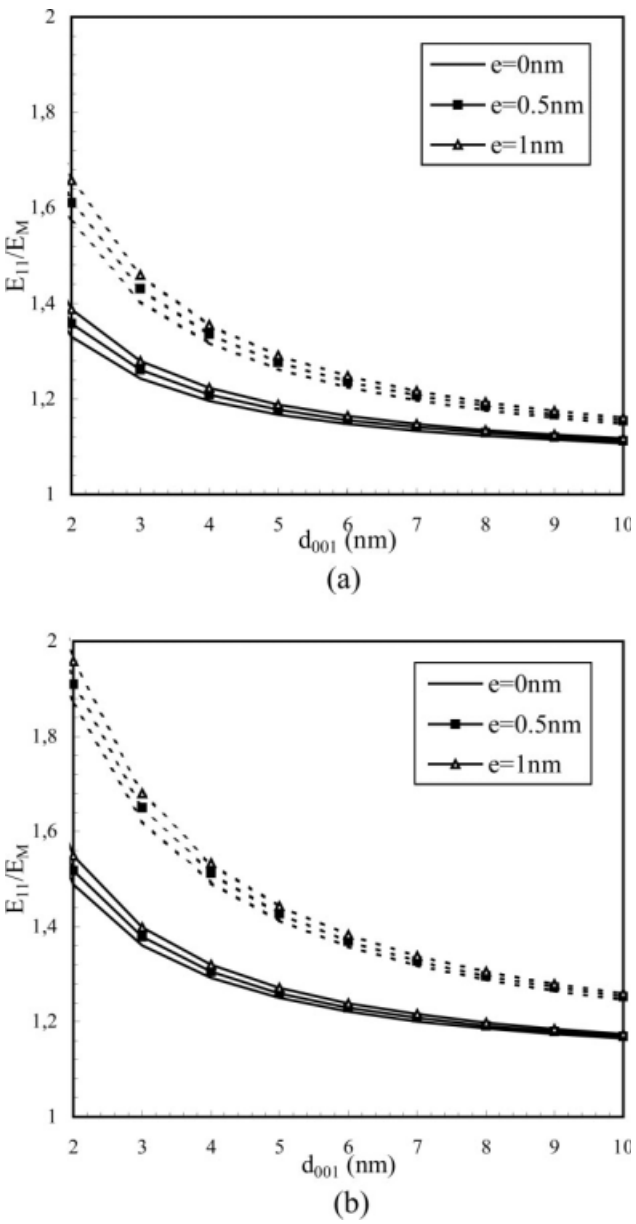

Figure 14 Effect of interlayer spacing on the overall Young's modulus (discontinuous lines: unidirectionally oriented particles, continuous lines: randomly oriented particles): (a) $E_M = 3000$ MPa, (b) $E_M = 1$ MPa.

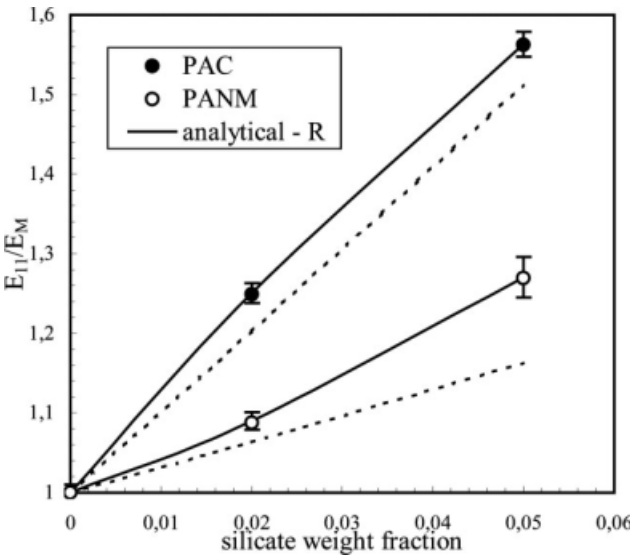

Figure 15 Comparison between analytical model (with randomly oriented particles) and experimental data of the overall Young's modulus of PAC and PANM nanocomposites (discontinuous lines: model without interphase, continuous lines: model with interphase).

value is higher than the 1.85 nm spacing before processing. The average number of silicate layers was taken equal to 4. The structural parameters of the intercalated silicate stack are assumed to be independent of weight fraction in the range of filler fractions investigated. The elastic modulus assigned to MMT silicate was 178 GPa. To our knowledge, there is no direct measurement technique of the elastic modulus of the confined polymer matrix in the intersilicate layers. To reduce the number of parameters, it is assumed to be the same as that of the matrix. To convert the clay weight fraction into particle volume fraction a density of 1.1 g/cm^3 was used for PA6.

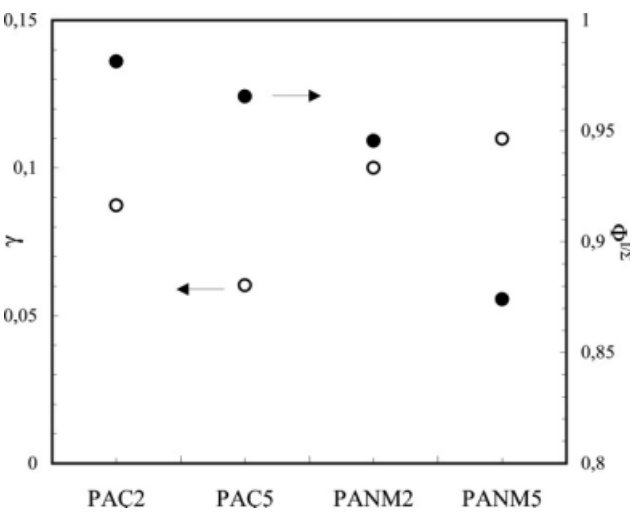

Figure 16 Interphase volume fraction inside the inclusion and γ parameter for PAC and PANM nanocomposites.

Predicted stiffness and experimental values are plotted in Figure 15 as a function of silicate weight fraction. When the interphase is not taken into account, a deviation between predictions and experimental results is shown. The influence of the interphase is then examined. The volume fraction of interphase was identified in the experimental part and it is given in Figure 5. The good dispersion of clay achieved in the PAC nanocomposites leads to a large amount of interphase. Indeed, at room temperature, the volume fraction of interphase inside the nanocomposite is 50.8% for PAC2 and 68.8% for PAC5. This corresponds to an interphase thickness around individually dispersed 1-nm thick platelets

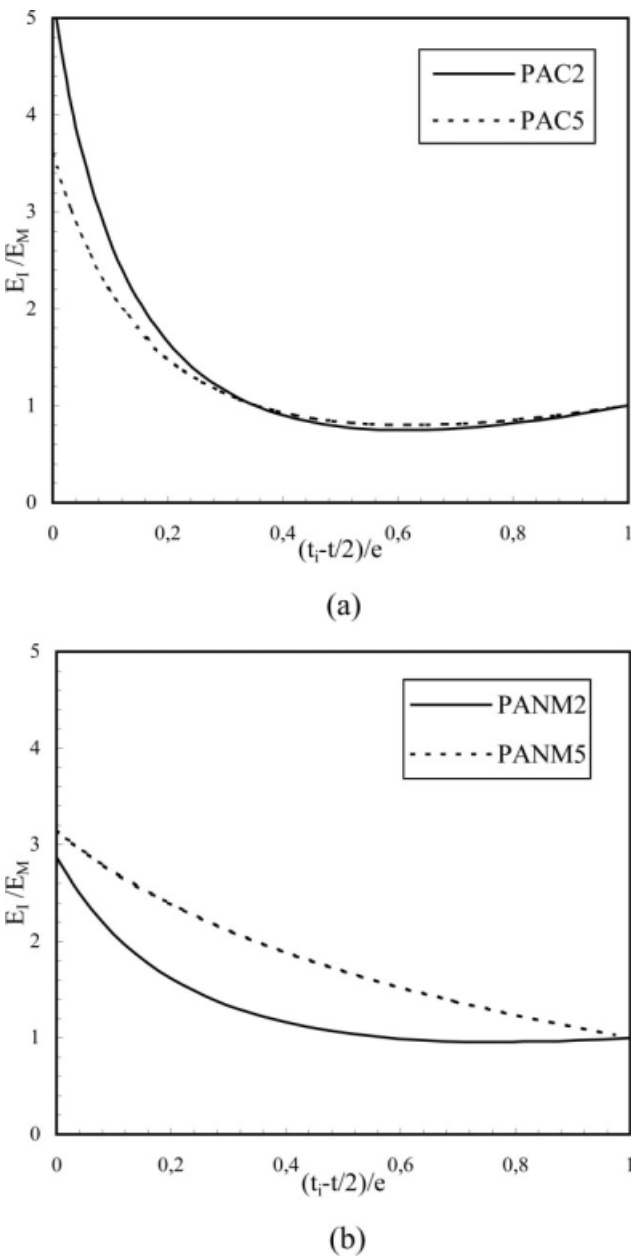

Figure 17 Variation of the stiffness in the interphase for (a) PAC and (b) PANM nanocomposites.

of about 3 nm for PAC2 and 2 nm for PAC5. Intercalated structure results in an increase of aspect ratio and a decrease of specific surface area, which results in a decreased amount of interphase. Note that intercalation also decreases the efficiency of the load transfer to the clay platelets. According to the volume fraction of interphase given in Figure 5, the interphase thickness around intercalated silicate stacks is about 12.5 nm for PANM2 and 7 nm for PANM5. Note that the average thickness of silicate stacks is 8.5 nm. Figure 16 presents the volume fraction of interphase inside the inclusion.

Because there is no direct experimental determination of the elastic modulus of the interphase in polymer/clay nanocomposites, the γ parameter appearing in the equations governing the stiffness evolution of the interphase is an unknown parameter, which is identified using the least-squares method. Let us remind that this parameter constitutes the only unknown parameter in the modeling. Considering the interphase, Figure 15 shows that the model can accurately capture the overall elastic modulus. The role of the interphase on overall stiffness enhancement is then clearly illustrated. However, clay still remains the dominant stiffening parameter. The determination of γ parameter offers the possibility to analyze the strength of the interactions between the clay and the matrix. The values of γ parameter are plotted in Figure 16 while the variation of stiffness in the interphase is presented in Figure 17.

CONCLUSION

PA6 nanocomposites were produced using an organoclay Cloisite 30B (PAC2 and PAC5) and an untreated clay Cloisite Na^+ (PANM2 and PANM5). The surface treatment of the clay significantly influences the nanocomposites structure as well as their mechanical properties. Confirmed by TEM observations, PAC and PANM nanocomposites exhibit exfoliated and intercalated states, respectively. The reinforcement effect of MMT was observed in DMA and tensile tests. The fraction of the interphase was estimated by means of DMA and DSC. Both analytical and numerical predictions of the overall nanocomposite stiffness were presented. To model the nanostructure, a multiscale approach was adopted. The interaction between clay and matrix was explicitly introduced in the analysis assuming the presence of an interphase between the two phases. Considering the interphase thickness as a characteristic length scale, the particle size effect was introduced in the model. At the nanometer scale, if an interphase is accounted for, an important particle size effect was pointed out. The geometric features of intercalated nanocomposites were examined. From the analytical point of view, the hierarchical morphology was introduced from the equivalent stiffness method in which the silicate stacks are replaced by homogeneous particles with constructed equivalent anisotropic stiffness. The effect of clay structural parameters was highlighted. When considering randomly oriented particles, there is no major enhancement of the nanocomposite modulus due to the morphological transition from intercalated to exfoliated state. RVE were generated to model various nanocomposites deformed in tension. The FE results correlated well with the analytical results. The model was used to evaluate the elastic modulus of systems experimentally investigated. Even if clay content is the dominant stiffening parameter, the contribution of the interphase is not negligible.

The model will be extended to the yield behavior. From the experimental point of view, nanoindentation may be considered to check the interphase features.

Region Nord Pas de Calais funding through ARCir program "polymer/clay nanocomposites" is gratefully acknowledged.

APPENDIX A

The components of Eshelby tensor for a spheroidal particle are[28]

$$S_{1111} = S_{2222} = \frac{3}{8(1-\nu_M)}\frac{\alpha^2}{\alpha^2-1} + \frac{1}{4(1-\nu_M)}\left[1-2\nu_M-\frac{9}{4(\alpha^2-1)}\right]f(\alpha) \quad (A.1)$$

$$S_{3333} = \frac{1}{2(1-\nu_M)}\left[1-2\nu_M+\frac{3\alpha^2-1}{\alpha^2-1} - \left(1-2\nu_M+\frac{3\alpha^2}{\alpha^2-1}\right)f(\alpha)\right] \quad (A.2)$$

$$S_{1122} = S_{2211} = \frac{1}{4(1-\nu_M)}\left[\frac{\alpha^2}{2(\alpha^2-1)} - \left(1-2\nu_M+\frac{3}{4(\alpha^2-1)}\right)f(\alpha)\right] \quad (A.3)$$

$$S_{1133} = S_{2233} = \frac{1}{2(1-\nu_M)}\frac{\alpha^2}{\alpha^2-1} - \frac{1}{4(1-\nu_M)}\left(1-2\nu_M-\frac{3\alpha^2}{\alpha^2-1}\right)f(\alpha) \quad (A.4)$$

$$S_{3311} = S_{3322} = -\frac{1}{2(1-\nu_M)}\left(1-2\nu_M+\frac{1}{\alpha^2-1}\right) + \frac{1}{2(1-\nu_M)}\left(1-2\nu_M+\frac{3}{2(\alpha^2-1)}\right)f(\alpha) \quad (A.5)$$

$$S_{1313} = S_{2323} = \frac{1}{4(1-\nu_M)} \times \left[1 - 2\nu_M - \frac{\alpha^2+1}{\alpha^2-1} - \frac{1}{2}\left(1 - 2\nu_M - \frac{3(\alpha^2+1)}{\alpha^2-1}\right) f(\alpha)\right] \quad \text{(A.6)}$$

$$S_{1212} = \frac{1}{4(1-\nu_M)} \times \left[\frac{\alpha^2}{2(\alpha^2-1)} + \left(1 - 2\nu_M - \frac{3}{4(\alpha^2-1)}\right) f(\alpha)\right] \quad \text{(A.7)}$$

in which α is the aspect ratio of the particle defined as the ratio between the thickness t and the length L and $f(\alpha)$ is given by

$$f(\alpha) = \begin{cases} \frac{\alpha}{(\alpha^2-1)^{3/2}}\left[\alpha(\alpha^2-1)^{1/2} - \cosh^{-1}\alpha\right] & \text{if } \alpha > 1 \\ \frac{\alpha}{(1-\alpha^2)^{3/2}}\left[\cos^{-1}\alpha - \alpha(1-\alpha^2)^{1/2}\right] & \text{if } \alpha < 1 \end{cases} \quad \text{(A.8)}$$

APPENDIX B

Parameters in eqs. (18) and (21) are expressed as

$$\eta_1 = \frac{\nu_{\text{silicate}}^2 E_{\text{gallery}}/E_{\text{silicate}} + \nu_{\text{gallery}}^2 E_{\text{silicate}}/E_{\text{gallery}} - 2\nu_{\text{silicate}}\nu_{\text{gallery}}}{\chi E_{\text{silicate}} + (1-\chi)E_{\text{gallery}}} \quad \text{(B.1)}$$

$$\eta_2 = \frac{\nu_{\text{silicate}}^2 G_{\text{gallery}}/G_{\text{silicate}} + \nu_{\text{gallery}}^2 G_{\text{silicate}}/G_{\text{gallery}} - 2\nu_{\text{silicate}}\nu_{\text{gallery}}}{\chi G_{\text{silicate}} + (1-\chi)G_{\text{gallery}}} \quad \text{(B.2)}$$

APPENDIX C

The relation between the particle weight fraction W_P and the particle volume fraction ϕ_P is given by the following expression:

$$\phi_P = \frac{1}{1 + \left(\frac{1}{W_P} - 1\right)\frac{\rho_P}{\rho_M}} \quad \text{(C.1)}$$

in which ρ_P and ρ_M are the densities of the particle and the matrix, respectively.

The particle weight fraction W_P can be related to the silicate weight fraction W_{silicate} by

$$W_P = \frac{\rho_P V_P}{\rho_{\text{silicate}} V_{\text{silicate}}} W_{\text{silicate}} = \frac{\rho_P}{\rho_{\text{silicate}}\chi} W_{\text{silicate}} \quad \text{(C.2)}$$

where ρ_{silicate} is the density of the silicate layer taken equal to 2.3 g/cm^3.[7]

In the case of a low weight fraction of silicate W_{silicate}, eq. (C.1) can be rewritten as[13]

$$\phi_P \approx \frac{\rho_M}{\rho_{\text{silicate}}\chi} W_{\text{silicate}} \quad \text{(C.3)}$$

References

1. Usuki, A.; Kojima, Y.; Kawasumi, M.; Okada, A.; Fukushima, Y.; Kurauchi, T.; Kamigaito, O. J Mater Res 1993, 8, 1179.
2. Kojima, Y.; Usuki, A.; Kawasumi, M.; Okada, A.; Fukushima, Y.; Kurauchi, T.; Kamigaito, O. J Mater Res 1993, 8, 1185.
3. Ray, S. S.; Okamoto, M. Prog Polym Sci 2003, 28, 1539.
4. Okada, A.; Usuki, A. Macromol Mater Eng 2006, 291, 1449.
5. Okamoto, M. Mater Sci Tech 2006, 22, 756.
6. Pavlidou, S.; Papaspyrides, C. D. Prog Polym Sci 2008, 33, 1119.
7. Masenelli-Varlot, K.; Reynaud, E.; Vigier, G.; Varlet, J. J Polym Sci Part B: Polym Phys 2002, 40, 272.
8. Tandon, G. P.; Weng, G. J. Polym Comp 1984, 5, 327.
9. Brune, D. A.; Bicerano, J. Polymer 2002, 43, 369.
10. Halpin, J. C.; Kardos, J. L. Polym Eng Sci 1976, 16, 344.
11. Luo, J. J.; Daniel, I. M. Comp Sci Tech 2003, 63, 1607.
12. Mori, T.; Tanaka, K. Acta Metall 1973, 21, 571.
13. Sheng, N.; Boyce, M. C.; Parks, D. M.; Rutledge, G. C.; Abes, J. I.; Cohen, R. E. Polymer 2004, 45, 487.
14. Wang, J.; Pyrz, R. Comp Sci Tech 2004, 64, 925.
15. Shelley, J. S.; Mather, P. T.; Devries, K. L. Polymer 2001, 42, 5849.
16. Ji, X. L.; Jing, J. K.; Jiang, W.; Jiang, B. Z. Polym Eng Sci 2002, 42, 983.
17. Wang, J.; Pyrz, R. Comp Sci Tech 2004, 64, 935.
18. Fornes, T. D.; Paul, D. R. Polymer 2003, 44, 4993.
19. Wu, Y. P.; Jia, Q. X.; Yu, D. S.; Zhang, L. Q. Polym Test 2004, 23, 903.
20. Weon, J. I.; Sue, H. J. Polymer 2005, 46, 6325.
21. Li, X.; Gao, H.; Scrivens, W. A.; Fei, D.; Thakur, V.; Sutton, M. A.; Reynolds, A. P.; Myrick, M. L. Nanotechnology 2005, 16, 2020.
22. Maksimov, R. D.; Gaidukovs, S.; Kalnins, M.; Zicans, J.; Plume, E. Mech Comp Mater 2006, 42, 235.
23. Jo, C.; Fu, J.; Naguib, H. E. Polym Eng Sci 2006, 46, 1787.

24. Wilkinson, A. N.; Man, Z.; Stanford, J. L.; Matikainen, P.; Clemens, M. L.; Lees, G. C.; Liauw, C. M. Comp Sci Tech 2007, 67, 3360.
25. Saber-Samandari, S.; Afaghi-Khatibi, A. Polym Comp 2007, 28, 405.
26. Hbaieb, K.; Wang, Q. X.; Chia, Y. H. J.; Cotterell, B. Polymer 2007, 48, 901.
27. Campoy, I.; Gomez, M. A.; Marco, C. Polymer 1998, 39, 6279.
28. Eshelby, J. D. Proc Roy Soc Lond 1957, 241, 376.
29. Hori, M.; Nemat-Nasser, S. Mech Mater 1993, 14, 189.
30. Ju, J. W.; Chen, T. M. Acta Mech 1994, 103, 103.
31. Liu, H. T.; Sun, L. Z. Acta Mater 2005, 53, 2693.
32. Tsai, S. W.; Hahn, H. T. Introduction to Composite Materials; Technomic Pub.: Lancaster, Pennsylvania, USA, 1980.
33. Tyan, H. L.; Wei, K. H.; Hsieh, T. E. J Polym Sci Part B: Polym Phys 2000, 38, 2873.
34. Lan, T.; Pinnavaia, T. J. Chem Mater 1994, 6, 2216.